Commun. Theor. Phys. **76** (2024) 065503 (17pp) https://doi.org/10.1088/1572-9494/ad393e

Persistent currents of ultrarelativistic plasma-encased endofullerene molecules entrapping a H atom

Mustafa Kemal Bahar

Department of Physics, Faculty of Science, Sivas Cumhuriyet University, 58140, Sivas, Turkey

E-mail: mussiv58@gmail.com

Received 27 December 2023, revised 26 March 2024
Accepted for publication 1 April 2024
Published 8 May 2024

Abstract

In this work, for the first time in the relevant literature, the persistent currents (PC) and induced magnetic fields (IMF) of an endofullerene molecule entrapping a hydrogen atom, under spherical confinement, are investigated. The endofullerene molecule is enclosed within a spherical region and embedded in a plasma environment. The plasma environment is depicted with the more general exponential cosine screened Coulomb potential, and its relevant effects are analyzed by considering plasma screening parameters. The relevant model for endohedral confinement is the Woods–Saxon confinement potential, which is compatible with experimental data. The effects of various forms of C_n are thoroughly elucidated via the analysis of the confinement depth, spherical shell thickness, the inner radius, and the smoothing parameters. To find the bound states in the spherically confined endofullerene, the decoupling of the second-order Dirac equation for the large and small components of the radial atomic wave functions is considered. The Dirac equation with the interaction potential is solved numerically by using the Runge–Kutta–Fehlberg method via the decoupling formalism. The influence of spin orientations on the PC and IMF is also elucidated. The effects of spherical confinement, plasma shielding, and the structural properties of the fullerene on the PC and IMF are thoroughly viewed. Moreover, under given physical conditions, the optimal ranges of these effects are determined.

Keywords: quantum plasma, endohedral fullerene, persistent current, ultrarelativistic interaction, induced magnetic field

(Some figures may appear in colour only in the online journal)

1. Introduction

Endofullerenes represent specialized structures within fullerene molecules, typically characterized by a spherical arrangement formed by carbon atoms, harboring different atoms or molecules within their interior. These structures often consist of atoms or molecules placed inside the fullerene shell, typically with an inner filling. Endofullerenes acquire unique properties due to the materials encapsulated within them [1, 2]. The inner filling significantly alters or enhances the electronic, magnetic, and chemical properties of endofullerenes. These properties enable diverse applications of endofullerenes, such as in nanotechnology, drug delivery, catalysis, and materials science [3–6]. These structures, by manipulating properties at the molecular level, could potentially play a significant role in various industrial fields in the future. Endofullerenes are complex exotic molecular structures that can be synthesized in different geometries, symbolized in terminology as $X@C_n$ [7]. The synthesis of endofullerenes is typically achieved using two main methods: endohedral metallofullerenes, or endohedral complementary amines. However, our focus in the present work leans more towards endofullerenes containing hydrogen atoms. The synthesis of hydrogen-containing endofullerenes generally involves the interaction of hydrogen plasma with carbon structures. This process typically occurs under high temperature and pressure conditions. One method involves the reaction of carbon structures (usually graphite or carbon

nanotubes) with hydrogen plasma, occurring within an environment where hydrogen gas is used to create a high-energy plasma. Carbon structures allow hydrogen atoms to interact within this plasma, enabling the incorporation of hydrogen into the carbon structures [8]. In this process, mechanisms such as the diffusion or absorption of hydrogen into carbon structures can play a role. This process facilitates the synthesis of hydrogen-containing endofullerenes by incorporating hydrogen into the carbon structures. The resulting structures can possess various properties, depending on the position and distribution of hydrogen within the endofullerene. Such hydrogen-containing endofullerenes have the potential to be used in various applications as hydrogen storage technologies and energy storage systems [9]. The properties and potential applications of endofullerenes stimulate in-depth investigations in this area and inspire new experimental/theoretical studies. Endofullerenes come in various types with different numbers of carbon atoms, exhibiting diverse geometric properties, such as their sizes and superficial features. By considering these differences, the C_n model is proposed in the present work to analyze characteristics such as the width, depth, thickness, and smoothing of endofullerenes. Theoretical studies on endofullerenes have predominantly focused on research areas such as the ionization potential, delocalizations, quantum information, photoionization, orbital distortion, and magnetic, optical, and thermal properties for the $X@C_n$ complex [10–16].

Plasma is a state typically composed of ionized gases found at high temperatures and energy levels. However, it can also be easily generated under atmospheric conditions. In this case, electrons stripped from the outer shells of atoms create ions and free electrons, allowing positively and negatively charged particles to move freely. Plasma is best characterized by ionized gases and is typically formed in conditions of high temperature, high pressure, or high electric fields. It can be produced not only in natural settings, such as the Sun and stars, but also in laboratories and industries. The high-energy level determines the many characteristics of plasmas. Due to these properties, plasmas find applications in various areas, such as lasers, semiconductor manufacturing, materials processing, space research, nuclear fusion, and a wide array of atomic and molecular interactions [17]. Plasmas play a significant role in applications within atomic and molecular physics. Processes such as electron collisions with atoms, and absorption and emission of photons form the basis of plasma physics. These processes can also vary under the influence of magnetic fields, highlighting the complex nature of plasmas that need to be studied and controlled [18, 19]. In this manner, the interactions of plasmas at the atomic and molecular levels, processes such as energy transfer and conversion, constitute a significant research area in modern physics and technology. Studies in this area have the potential to lead to groundbreaking innovations in various fields, such as the production of new materials, space exploration, and energy generation [20]. The plasma environment provides optimal conditions for exciting an atom or molecule. However, within this excitation process, processes such as oscillator strengths, phase shifts, localizations of energy levels, and photoionization can be managed through the plasma shielding function. In this context, the $H@C_n$ molecule is considered embedded within the plasma to experience a strong shielding effect in a quantum plasma. When modeling quantum plasma interactions, our work considers a more general exponential cosine screened Coulomb (MGECSC) potential. For more details about this potential, please refer to [21–23]. Plasma-encased endofullerene systems are a significant research subject for two reasons. Firstly, the plasma environment is highly functional in synthesizing or modifying endofullerenes. The high temperature and energy levels within plasma allow carbon structures to react in various ways. Under these conditions, carbon structures can form different molecular configurations under the influence of plasma. Alternatively, free atoms or molecules within the plasma can penetrate the interior of carbon structures and reside within endofullerenes. The formation of such endofullerenes is being investigated in fields such as materials science, nanotechnology, and plasma chemistry, exploring their potential applications. The second reason is that plasmas' shielding properties can be utilized to control certain spectral, electronic, optical, and spectroscopic characteristics of endofullerenes. The energy levels, oscillator strengths, mean excitation energy, photoionization dynamics, and static dipole polarizability of a hydrogen atom enclosed in an endohedral cage under the influence of a weak plasma interaction have been examined using a finite difference approach [24]. In the present work, the C_n model for endohedral confinement has been considered within the framework of the Woods–Saxon potential, taking into account the well depth V_0, inner radius R_0, thickness D, and smoothing parameter γ. This research distinctly elucidates the interaction between plasma and an endohedral molecule, suggesting that plasma plays an effective role in the physical properties of the aforementioned endohedral molecule. According to the overall findings of the study, there is strong competition between the effects of plasma interaction and the static endohedral cavity, thereby altering the electronic characteristics of the system. Motivated by the functionality provided by the plasma shielding effect, a similar study has been conducted in nonideal classical plasma [25], explaining the effects of a nonideal classical plasma environment on the photoionization dynamics of hydrogen-containing endofullerene molecules. In this study as well, significant features of both components of the plasma–endofullerene system have been identified.

The change in the aforementioned physical properties of the plasma–endofullerene system has been sufficiently motivating in the study of quantities such as the persistent current (PC) and induced magnetic field (IMF). In atoms, molecular systems, and artificially low-dimensional structures such as quantum dots, electric currents arising from atomic orbits and the associated induced magnetic fields are fundamentally linked to the movement of electrons. Electrons revolving around the atom's nucleus carry momentum due to their speed within their orbits, constituting moving charges that generate a current. Electrons orbiting in a loop correspondingly produce a magnetic field associated with that current, following Ampere's law of circulating currents around a moving charge.

These orbital currents create magnetic fields at the atomic level, influencing the magnetic properties of atoms and molecules. Particularly, these effects may involve directing or altering magnetic moments, forming the basis for many magnetic materials and devices. The magnetic effects of orbital currents find applications in various fields, ranging from medical imaging devices, such as magnetic resonance imaging, to magnetic memories and sensors. The PC at the atomic level and the resultant IMF play a significant role in various aspects of modern technology, emphasizing the crucial importance of precise control over them [26–29]. Various physical factors may be involved in the formation and control of the PC and IMF in atomic systems. In this context, twisted lights have recently garnered attention because they involve the interaction between the orbital angular momentum and the spatial modes of the electromagnetic field. What makes twisted lights intriguing is their ability to alter significant steady currents, even in situations where there are no externally applied magnetic fields [30–32]. Such beams provide a significant advantage in that the dynamics of the laser–matter interaction do not depend on traditional selection rules, and the PC and IMF can then be generated simply by changing the orbital angular momentum index of the beam. It should be pointed out that an optical vortex has a significant effect on the charge current and magnetism in fullerene [31]. The Rashba spin–orbit interaction is a significant factor in the generation and modification of the PC and IMF due to the spin-twisting itinerant motion of electrons. It stabilizes the alternating motion of electrons by fixing their spins [32]. Another significant factor affecting the PC and IMF is the use of laser pulses. In this manner, time-delayed light pulses on nanoscopic and mesoscopic ring structures [33] and picosecond-shaped laser pulses on valley currents and magnetization in graphene rings [34, 35] establish a functional mechanism. Taking into account electron spin, the effectiveness of short intense circularly polarized π laser pulses on the PC and IMF of hydrogen atoms and certain ions has been thoroughly explained [36]. Several factors can have a significant impact on the PC and IMF in atomic systems. Exploring these factors not only guides experimental researchers, but also motivates theoretical studies to test new models and mechanisms. In this context, some effects, such as noncentral interactions, laser pulses, external magnetic fields, external electric fields, and spherical confinement, offer significant outcomes [37–40]. The common outcome of most of these studies is to elucidate how the PC and IMF can be modified by external influences. These explanations benefit the development of new opto-magnetic devices and magneto-optic materials, allowing the manipulation of many physical quantities that are sensitive to magnetic fields at the subatomic level. Endofullerenes can exhibit different magnetic properties, depending on the filling material inside them. This can be controlled by selecting the interior fillings or through external influences (such as external magnetic fields). Moreover, it can lay the groundwork for magnetic storage systems and spintronic applications. Endofullerenes could serve as potential building blocks for nanoscale electronic devices. These systems enable the control of nano-sized currents and magnetic fields. Research in these fields can be seen as significant steps toward understanding and controlling magnetic specifications of endofullerenes, and translating them into applications. This could lead to significant discoveries and advancements in materials science, nanotechnology, and magnetism fields. Considering the advantages of plasma in the synthesis of endofullerenes, as mentioned earlier, and the spectral properties that are modifiable by plasma's screening effects, the analysis of PC and IMF in plasma-encased endofullerene molecules is highly motivating.

The spins of electrons result in magnetic moments, influencing the formation of the PC and IMF in atomic systems. Spin is associated with the PC, and spin-carrying currents can have an impact on magnetic moments. Such currents play a significant role in the design of spintronic devices and magnetic storage systems [41]. On the other hand, the PC creates spin-circulation effects. This is when electrons rotate around their spin, parallel or antiparallel to charge currents. Spin–orbit coupling affects the electronic properties of the material and the behavior of carriers. Furthermore, in certain topological materials, there are connections between the spins and orbital motions of electrons [42]. For these reasons, the spin effects of charge currents are regarded as a significant area of research and application in fields such as materials science, magnetism, and spintronics. Therefore, this study will provide a relativistic examination by considering the spin effects within the Dirac formalism. The expectation from this study is to elucidate the effects of relativistic impacts and spin orientations on the PC and IMF covering plasma effects, endofullerene encapsulation, and spherical confinement. In doing so, experienced models and theoretical procedures will be utilized to parametrize these effects.

The study is organized as follows: in section 2, the model and theoretical formalism are presented. Section 3 elucidates the obtained results. Section 4 is dedicated to a brief summary and conclusion of the work.

2. Theoretical model and procedure

For atomic systems exhibiting spherical symmetric interactions, the time-independent Dirac Hamiltonian in atomic units reads as

$$H_{\mathrm{D}} = c\boldsymbol{\alpha}.\boldsymbol{p} + (\beta - I)c^2 + V(r), \tag{1}$$

where $V(r)$ is the spherical symmetric potential, $\boldsymbol{\alpha}$ and β are four-component matrices in standard Dirac–Pauli notation, I is a 4×4 unity matrix, and c is the light speed. Finding the eigenvalues and eigenvectors of the Dirac Hamiltonian to investigate relativistic effects is quite challenging due to its mathematical complexity. Additionally, the Dirac equation can be analytically solved for only a few potentials. To determine the eigenvalues and eigenvectors of the Dirac Hamiltonian with central potential, one must perform separation of the variables in the relevant Dirac equation, and this is where the real difficulty begins. The series of operations, considering the angular momentum ($\hat{J}$) and parity operator ($\hat{P}$) that commute with the Hamiltonian with respect

to the center of the coordinate system, results in coupled differential equations for radial wave functions [43]. However, considering the separability of the Dirac equation, highly functional and well-established formalisms have been developed for obtaining two decoupled second-order differential equations in the analysis of the Dirac equation, such as the SUSY approach [44], and coupling the relativistic equation into large and small components by squaring the Dirac Hamiltonian [45, 46]. Within the modification of spin and angular variables, for an atomic system with the potential interaction $V(r)$, the Dirac second-order equation in atomic units reads as follows [47–51]

$$\left[\Upsilon I' + \frac{1}{r^2}\Delta\right]\begin{pmatrix} G_\kappa \\ F_\kappa \end{pmatrix} = 0, \tag{2}$$

with

$$\Upsilon = -\frac{\mathrm{d}^2}{\mathrm{d}r^2} + \frac{\kappa^2}{r^2} + 2(V(r) - E) - \frac{1}{c^2}(V(r) - E)^2, \tag{3}$$

$$\Delta = \begin{pmatrix} -\kappa & -\dfrac{r^2}{c}\dfrac{\mathrm{d}V(r)}{\mathrm{d}r} \\ \dfrac{r^2}{c}\dfrac{\mathrm{d}V(r)}{\mathrm{d}r} & \kappa \end{pmatrix}, \tag{4}$$

while E is the electron energy as the difference between the total and rest energy, and G_κ, F_κ are, respectively, the large and small component radial functions, I' is the 2×2 unit matrix. The relativistic momentum quantum number κ states are $\kappa = \mp(j + \frac{1}{2})$ and $j = \ell \mp \frac{1}{2}$ in consideration of the orbital and total angular momentum quantum number ℓ and j, in which the mathematical formalism here works as $\kappa = -\ell$ for $j = \ell - \frac{1}{2}$ and $\kappa = \ell + 1$ for $j = \ell + \frac{1}{2}$. The following nonunitary transformation matrix and $r-$independent when considering $r^2\mathrm{d}V(r)/\mathrm{d}r = \eta \equiv$ constant, is identified when considering Δ matrix elements

$$M = s\begin{pmatrix} 1 & -\dfrac{1}{c}\dfrac{\eta}{\kappa + \Lambda} \\ -\dfrac{1}{c}\dfrac{\eta}{\kappa + \Lambda} & 1 \end{pmatrix}, \tag{5}$$

with s, which is a constant, and

$$\Lambda = \kappa\sqrt{1 - \frac{1}{\kappa^2 c^2}\left(r^2\frac{\mathrm{d}V(r)}{\mathrm{d}r}\right)^2}. \tag{6}$$

The relevant equations can be decoupled, by employing M and Λ, as well as the relation $M^{-1}\Delta M$

$$M^{-1}\Delta M = \begin{pmatrix} -\Lambda & 0 \\ 0 & \Lambda \end{pmatrix}, \tag{7}$$

which, in turn, provides the following coupling form of the second-order Dirac equation

$$\left[\Upsilon \pm \frac{\Lambda}{r^2}\right]F_\pm(r) = 0, \tag{8}$$

where $F_\pm(r)$ are scalar amplitudes. Equation (8) is solved by employing the Runge–Kutta–Fehlberg method. For details, please refer to [52].

In a quantum plasma environment, an encapsulated H atom within a C_n fullerene is surrounded by a spherical encompassement with R_0 radius. When a relativistic hydrogen atom is compressed to a spherical region with R_0 radius under a pressure P, significant changes are observed in the atom's spectral energies. Therefore, studying the cases where the bound-state energy levels of the hydrogen atom change under such ultrarelativistic conditions is suitable for the ultrarelativistic condition and is important in understanding these situations. The pressure P referred to the case of when considering plasma-encased $H@C_n$ under the spherical confinement

$$P = (4\pi R_0^3)^{-1}(E_0 - \langle V\rangle), \tag{9}$$

where E_0 is the ground state energy, and $\langle V\rangle$ is the estimated value of the potential energy. In this case, the spherical confinement potential reads

$$V_\mathrm{c}(r) = \begin{cases} 0, & \text{if } r < R_0 \\ \infty, & \text{if } r \geqslant R_0 \end{cases}. \tag{10}$$

The Woods–Saxon potential model, which is one of the suitable models for static trapping hydrogen atoms within a fullerene that is compatible with experimental data, is considered [53]. Then, the static endohedral entrapping potential model is given by [54]

$$V_\mathrm{EC}(r) = \frac{V_0}{1 + \exp(-\frac{r - (R_\mathrm{c} + D)}{\Gamma})} - \frac{V_0}{1 + \exp(-\frac{r - R_\mathrm{c}}{\Gamma})}, \tag{11}$$

where V_0 is the confinement strength, D is the spherical shell thickness, R_c is the inner radius of the endohedral cage, and Γ is the smoothing parameter. The strong screening effect of quantum plasma, complicated correlations in the plasma environment, and various perturbations can be most comprehensively modeled using the MGECSC potential [21, 23, 55]. This model is presented as follows:

$$V_\mathrm{MGECSC}(r) = -\frac{Ze^2}{4\pi\varepsilon_0 r}(1 + br)\exp(-r/\lambda)\cos(ar/\lambda), \tag{12}$$

where $Z = 1$ for the hydrogen atom, and a, b, and λ are the plasma shielding parameters. In such a scenario, by considering the combined effects of the spherical encompassement, quantum plasma, and endohedral trapping, the total interaction potential in equation (1) is written as follows:

$$V(r) = V_\mathrm{MGECSC}(r) + V_\mathrm{EC}(r) + V_\mathrm{c}(r). \tag{13}$$

Under these conditions, within the context of spherical symmetry motivation, the eigenvalue equation that needs to be solved is $H_\mathrm{D}\Psi_{n\kappa m}(r, \theta, \varphi) = E\Psi_{n\kappa m}(r, \theta, \varphi)$, where $\Psi_{n\kappa m}(r, \theta, \varphi)$ is written, by considering large and small component radial functions, as

$$\Psi_{n\kappa m}(r, \theta, \varphi) = \begin{bmatrix} G_{n\kappa}(r) & \chi_{\kappa m}(\theta, \varphi) \\ \mathrm{i}F_{n\kappa}(r) & \chi_{-\kappa m}(\theta, \varphi) \end{bmatrix}, \tag{14}$$

where $\chi_{\kappa m}(\theta, \varphi)$ is the spin angular function, expressed as

$$\chi_{\kappa m}(\theta, \varphi) = \sum_{\sigma=\pm\frac{1}{2}} < \ell m - \sigma\frac{1}{2}\sigma|\ell\frac{1}{2}jm > Y_{\ell}^{m-\sigma}(\theta, \varphi)\phi^{\sigma}, \tag{15}$$

where $<\ell m - \sigma\frac{1}{2}\sigma|\ell\frac{1}{2}jm>$ are the Clebsch–Gordan coefficients, $Y_{\ell}^{m-\sigma}(\theta, \varphi)$ are the spherical harmonics, and ϕ^{σ} is the spin functions as

$$\phi^{\frac{1}{2}} = \begin{pmatrix}1\\0\end{pmatrix}, \phi^{-\frac{1}{2}} = \begin{pmatrix}0\\1\end{pmatrix}, \tag{16}$$

and n, m are the principle quantum number and the projection of the angular quantum number j, on the $z-$axis, respectively.

When considering the $\Psi_{n\kappa m}(r, \theta, \varphi)$ state, the probability current density is described as

$$\vec{J}_{n\kappa m}(r, \theta, \varphi) = \frac{\mathrm{i}\hbar}{2m_e}[\Psi_{n\kappa m}\nabla\Psi^{\star}_{n\kappa m} - \Psi^{\star}_{n\kappa m}\nabla\Psi_{n\kappa m}]. \tag{17}$$

With e being the electron charge, the orbital charge currents and induced magnetic field are depicted in the following form

$$I_{n\kappa m} = -e\int_0^{\pi}\int_0^{R_0} r\vec{J_{n\kappa m}}(r, \theta, \phi)\mathrm{d}r\mathrm{d}\theta\mathrm{d}\vec{\phi}, \qquad (\mathrm{m} \neq 0), \tag{18}$$

$$\vec{B}_{n\kappa m}(\vec{r}) = -\frac{\mu_0 e}{4\pi}\int\frac{\vec{J_{n\kappa m}}(\vec{r}) \times (\vec{r} - \vec{r'})}{|\vec{r} - \vec{r'}|^3}\mathrm{d}^3r', \tag{19}$$

where μ_0 is the vacuum permeability. For details, please refer to [56–58].

3. Results and discussion

In this study, we analyze the charge-current generations (PC: I (mA)) and IMF (B(T)) of spherical confined quantum plasma-encased $H@C_n$ within the framework of relativistic formalism. This analysis involves the effects of eight parameters: plasma shielding parameters (λ, b, and a), endofullerene static encompassement parameters (V_0, D, R_c, and Γ), and the spherical confinement radius (R_0). Additionally, the impact of spin orientations is examined. The methodology employed in the study has been tested by comparing its results with those of other studies under certain limits. In plasma environments modeled by the MGECSC potential for cases in the absence of endohedral encapsulation ($V_0 = 0$) and without spherical confinement ($R_0 \to 0$), the relativistic bound-state energies of the embedded hydrogen atom has been compared with the results produced by the direct perturbation method [59]. A perfect agreement between the relativistic bound-state energies in all relevant tables in [59] for $Z = 1$ and our results has been observed. Additionally, when considering the $b = 0$ and $b = a = 0$ limits in the MGECSC potential, a very good agreement has been found between our relativistic results for the ECSC and SC potentials and the nonrelativistic results produced by the Ritz method [60] and the $1/N$ method [61]. These observed numerical agreements are important and motivating for testing the employed methodology. Figure 1 presents the interaction potential profiles given in equation (13). Except for the profile in panel-h, all synchronized wave functions in the other profiles are oriented towards spin up. As depicted in figure 1(a), the variation of λ in the range of $0-150a_0$ has a more pronounced effect in the weak regime of λ. An increase in λ in this weak regime makes the interaction potential more attractive. Table 1 shows the variation of the energy values of some quantum states synchronized with the parameter set of figure 1(a) as a function of λ. The attractiveness caused by λ in the interaction potential is also reflected in the localization of bound-state energies. As expected, an increase in λ in weak regimes significantly reduces the localization of bound states, followed by a subsequent stability in later increments of λ (See table 1). The dynamics of bound-state localizations are the primary factors influencing the PC (I) and IMF (B). Figure 2 depicts the variation of the PC and IMF as a function of λ. As seen in figure 2, an increase in λ within the range of $0-30a_0$ initially leads to a noticeable decrease in the PC and IMF, followed by a subsequent stabilization. Figure 3 is synchronized with figure 2 and shows the radial density probabilities (RDP) of $2p$, $3d$, and $4f$ states for three different values of λ. Due to the intensified interaction potential as λ increases, the RDP of bound states decreases, leading to a decrease in I and B (see figure 3). The most pronounced response to the λ change is observed in the $2p$ state, resulting in the most dynamic effects in the $I-B$ characteristics within the $2p$ state.

Figure 1(b) depicts the interaction potential profile as a function of the plasma shielding parameter b and radial variable r. As observed, an increase in b enhances the attractiveness of the interaction potential, stabilizing the system concerning bound states. Table 2 illustrates the energy values of certain quantum states for the variation of b within $0 - 2.5/a_0$, when considering spin orientations. An increase in b leads to a more attractive interaction potential, resulting in a noticeable decrease in the localization of bound states. However, while the increase in the b parameter produces significant outcomes on energy levels, its effect on the PC and IMF is weak (See figure 4). Apart from the $2p$ level, the influence of b on the PC and IMF is quite uncertain in other states. Nevertheless, there is a remarkable effect of spin orientation on the values of I and B. Even though b has a strong impact on localizations, its weak effect on the $I-B$ characteristics is somewhat unusual. However, as seen in figure 5(a), an increase in b mildly enhances the RDP of $2p$, consequently leading to a slight increase in the PC and IMF for the $2p$ level. Similar elucidations hold true for the $3d$ and $4f$ states as well.

Figure 1(c) explains the effects of the plasma parameter a on the interaction potential. In this quantum system encompassed within a spherical region of radius R_0, there are no observable oscillations due to the a parameter, resulting in a weak repulsion. This weak repulsion leads to a decrease in the strength of the interaction potential, causing an inclination towards increased localization of bound states (See table 3). The weak impact of a on energy levels is reflected in the PC and IMF, as depicted in figure 6. An increase in a, most notably in the $2p$ state, causes a slight increase in the PC and

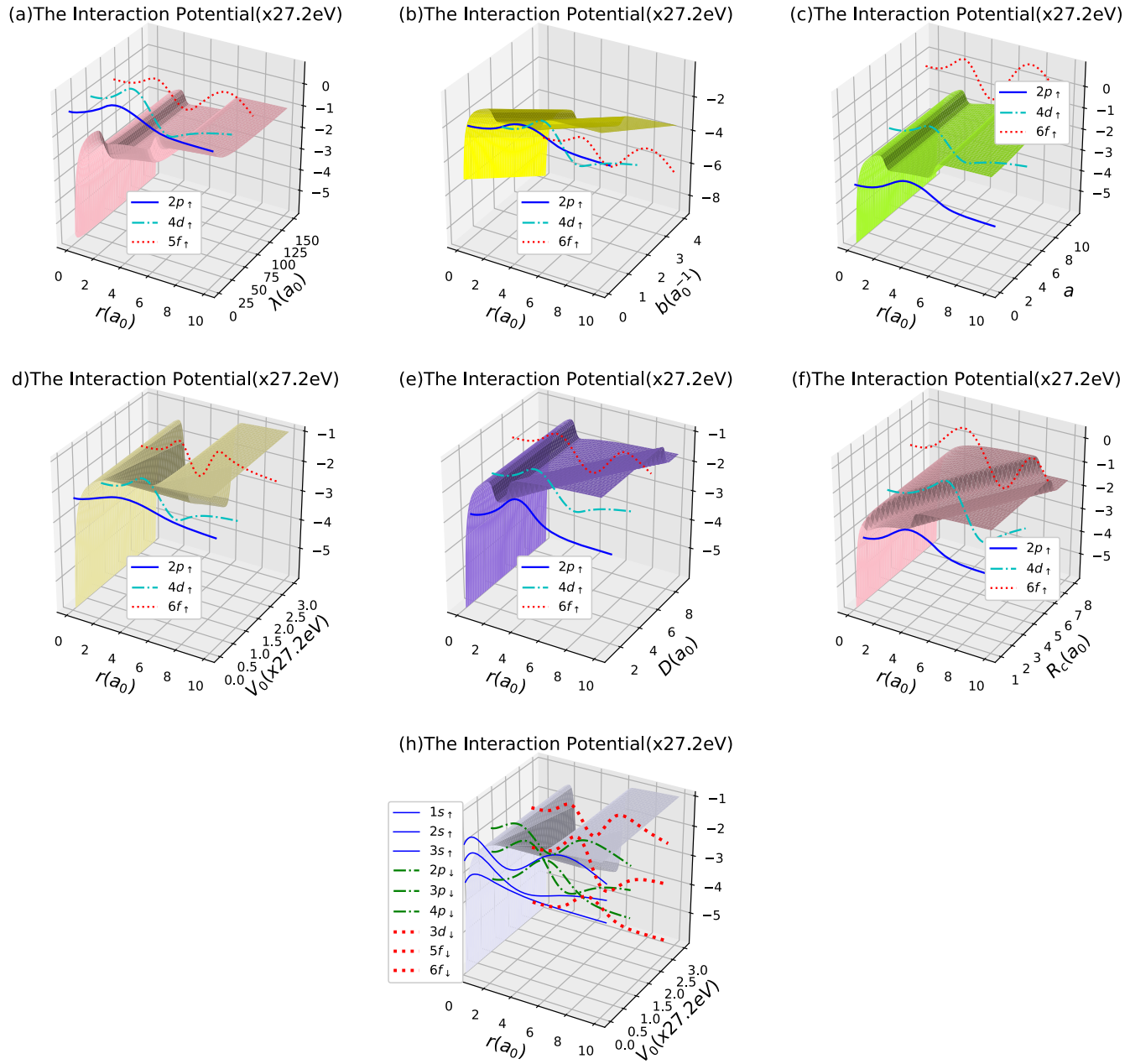

Figure 1. The interaction potential as the plasma plus endofullerene cage confinement and the relevant localized $2p-$, $4d-$, $6f-$ wave functions for: (**a**) $b = 1/a_0$, $a = 1$, $V_0 = 20$ eV, $D = 3.5a_0$, $R_c = 2.5a_0$, $\Gamma = 0.1a_0$, and $R_0 = 10a_0$ as a function of r and λ; (**b**) $\lambda = 80a_0$, $a = 1$, $V_0 = 20$ eV, $D = 3.5a_0$, $R_c = 2.5a_0$, $\Gamma = 0.1a_0$, and $R_0 = 10a_0$ as a function of r and b; (**c**) $\lambda = 80a_0$, $b = 1/a_0$, $V_0 = 20$ eV, $D = 3.5a_0$, $R_c = 2.5a_0$, $\Gamma = 0.1a_0$, and $R_0 = 10a_0$ as a function of r and a; (**d**) $\lambda = 80a_0$, $b = 1/a_0$, $a = 1$, $D = 3.5a_0$, $R_c = 2.5a_0$, $\Gamma = 0.1a_0$, and $R_0 = 10a_0$ as a function of r and V_0; (**e**) $\lambda = 80a_0$, $b = 1/a_0$, $a = 1$, $V_0 = 20$ eV, $R_c = 2.5a_0$, $\Gamma = 0.1a_0$, and $R_0 = 10a_0$ as a function of r and D; (**f**) $\lambda = 80a_0$, $b = 1/a_0$, $a = 1$, $V_0 = 20$ eV, $D = 3.5a_0$, $\Gamma = 0.1a_0$, and $R_0 = 10a_0$ as a function of r and R_c; (**g**) $\lambda = 80a_0$, $b = 1/a_0$, $a = 1$, $V_0 = 20$ eV, $D = 3.5a_0$, $R_c = 2.5a_0$, and $R_0 = 10a_0$ as a function of r and Γ; (**h**) $\lambda = 80a_0$, $b = 1/a_0$, $a = 1$, $D = 3.5a_0$, $R_c = 2.5a_0$, and $R_0 = 10a_0$ as a function of r and V_0, with some of the relevant $s-$, $p-$, $d-$, and $f-$ wave functions with spin down.

IMF in other quantum states as well. This is because the RDP of $2p$, $3d$, and $4f$ states mildly increases as a increases (see figure 7). While the spin orientation does not alter the general character of I and B, there is a notable difference between up and down states, consistent with other findings. Figure 1(d) elucidates the variation in the interaction potential as a result that the depth of the endohedral cage increases. It is evident that as V_0 increases, the encompassing effect of the interaction potential also rises. Consequently, a decrease in the energy levels of all bound states is expected, which is distinctly confirmed in table 4. The outcomes derived from the $2p$ level in the $I-B$ characteristics differ from those originating from $3d$ and $4f$. As the strength of the endohedral capsulation increases, there is a tendency for I_{2p} and B_{2p} to decrease while the others tend to increase, except for a slight initial increase (see figure 8). A more detailed analysis is needed to understand the reason behind this pattern. In figure 9, the RDP for $2p$, $3d$, and $4f$ are shown for cases

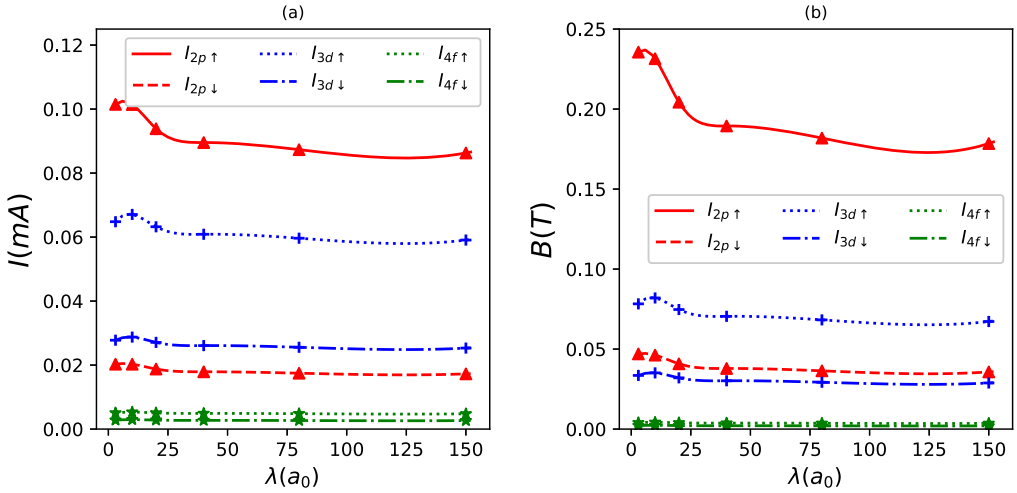

Figure 2. Persistent currents (a) and induced magnetic fields (b) as a function of λ for some quantum states in synchronization with the parameter set in figure 1(a).

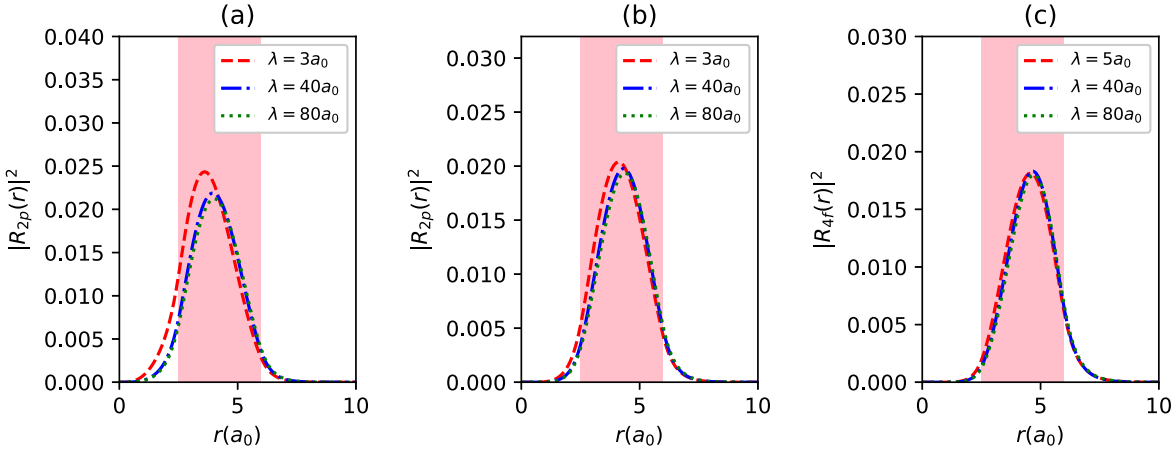

Figure 3. The radial density probabilities of $2p$ (a), $3d$ (b) and $4f$ states (c) with spin up for different λ values in synchronization with the parameter set in figure 2, as a function of r. The colored regions are the endohedral cage locations.

Table 1. Energy values for the λ-change variations of some quantum states in synchronization with the parameter set in figure 1(a).

	$\lambda(a_0)$					
Energy (eV)	3	10	20	30	50	100
$-E_{1s}$	23.369 184	38.704 208	43.723 837	45.616 53	47.205 723	48.437 189
$-E_{2p\uparrow}$	16.129 887	34.313 389	40.400 069	42.591 642	44.394 841	45.771 928
$-E_{2p\downarrow}$	16.131 188	34.314 721	40.401 542	42.593 187	44.396 454	45.773 599
$-E_{3d\uparrow}$	11.740 014	29.964 451	36.399 876	38.722 676	40.633 287	42.091 242
$-E_{3d\downarrow}$	11.741 007	29.965 421	36.400 953	38.723 804	40.634 461	42.092 453
$-E_{4f\uparrow}$	6.663 161	24.726 202	31.475 002	33.922 509	35.937 320	37.474 900
$-E_{4f\downarrow}$	6.664 184	24.727 182	31.476 073	33.923 620	35.938 475	37.476 074
$-E_{5g\uparrow}$		18.855 542	25.889 311	28.455 147	30.570 619	32.186 171
$-E_{5g\downarrow}$		18.856 632	25.890 469	28.456 333	30.571 829	32.187 398

without endohedral capsulation and for $V_0 = 20$ eV and $V_0 = 80$ eV. With regard to the $2p$ state, the electron's RDP not only moves away from the orbital center ($r = 0$) but also increases in a more stable manner. While $\vec{J}$ is the primary factor for persistent currents, it alone is not sufficient. As the electron localizes farther from the orbital center, the PC decreases. In this regard, for the $2p$ state, it could be said that the influence of the electron moving away from the orbital center on the I–B characteristics is more dominant compared to the increase in the RDP. For I_{3d} and B_{3d}, as the strength of the endohedral cage increases, the electron moves closer to the orbital center and the RDP increases. This leads to a

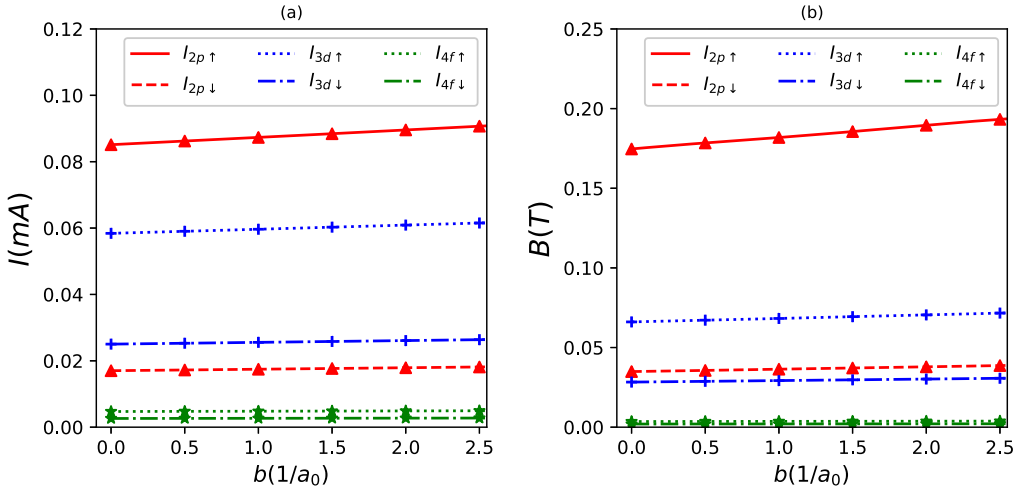

Figure 4. Persistent currents (a) and induced magnetic fields (b) as a function of b for some quantum states in synchronization with the parameter set in figure 1(b).

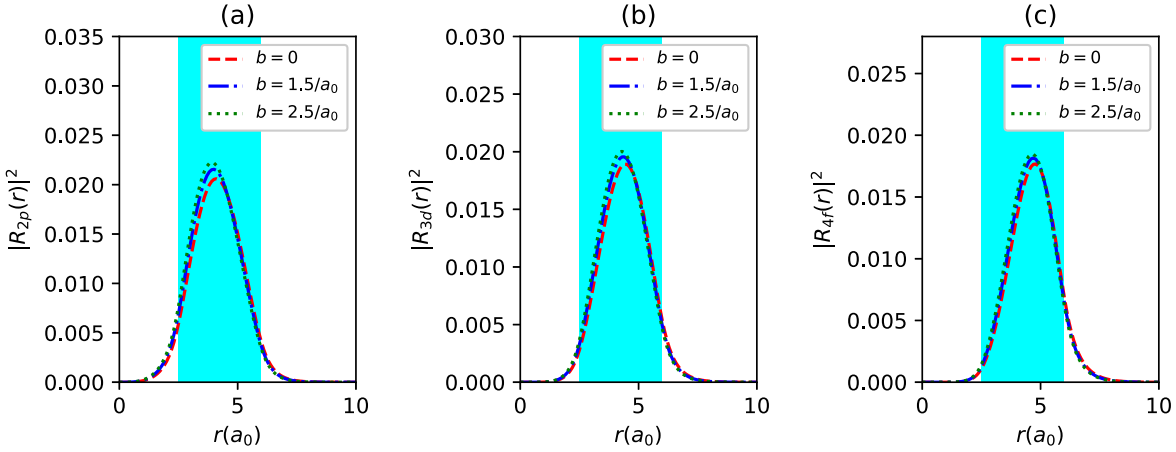

Figure 5. The radial density probabilities of $2p$ (a), $3d$ (b) and $4f$ states (c) with spin up for different b values in synchronization with the parameter set in figure 4, as a function of r. The colored regions are the endohedral cage locations.

Table 2. Energy values for the b-change of some quantum states in synchronization with the parameter set in figure 1(b).

	$b(a_0^{-1})$					
Energy (eV)	0	0.5	1	1.5	2	2.5
$-E_{1s}$	22.135 896	35.126 214	48.126 379	61.136 746	74.157 680	87.189 554
$-E_{2p\uparrow}$	19.603 685	32.512 469	45.425 905	58.343 962	71.266 607	84.193 810
$-E_{2p\downarrow}$	19.605 418	32.514 162	45.427 561	58.345 581	71.268 193	84.195 362
$-E_{3d\uparrow}$	16.003 262	28.862 127	41.725 028	54.591 926	67.462 782	80.337 562
$-E_{3d\downarrow}$	16.004 513	28.863 354	41.726 230	54.593 104	67.463 937	80.338 695
$-E_{4f\uparrow}$	11.466 867	24.275 925	37.088 719	49.905 199	62.725 317	75.549 028
$-E_{4f\downarrow}$	11.468 070	24.277 109	37.089 886	49.906 348	62.726 448	75.550 143
$-E_{5g\uparrow}$	6.257 403	19.016 984	31.780 344	44.547 389	57.318 036	70.092 208
$-E_{5g\downarrow}$	6.258 648	19.018 218	31.781 567	44.548 601	57.319 236	70.093 397

significant increase in both the PC and IMF. This increase results in the same outcome for $4f$ as well. However, for quantum levels such as $4f$, which are farther from the orbital center, the change in the PC and IMF is not clearly visible due to the scale of the graph in figure 8.

Figure 1(e) illustrates the confinement effect of the interaction potential as a function of the endohedral enclosure width (D) and the radial variable (r). The increase in D yields significant outcomes on quantum levels. The impact of the endohedral capsulation width on the localizations of quantum

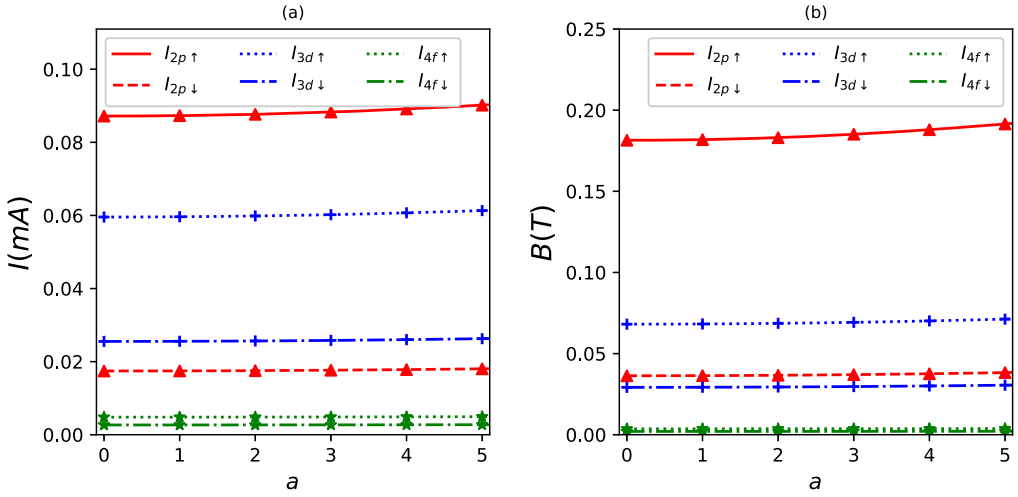

Figure 6. Persistent currents (a) and induced magnetic fields (b) as a function of a for some quantum states in synchronization with the parameter set in figure 1(c).

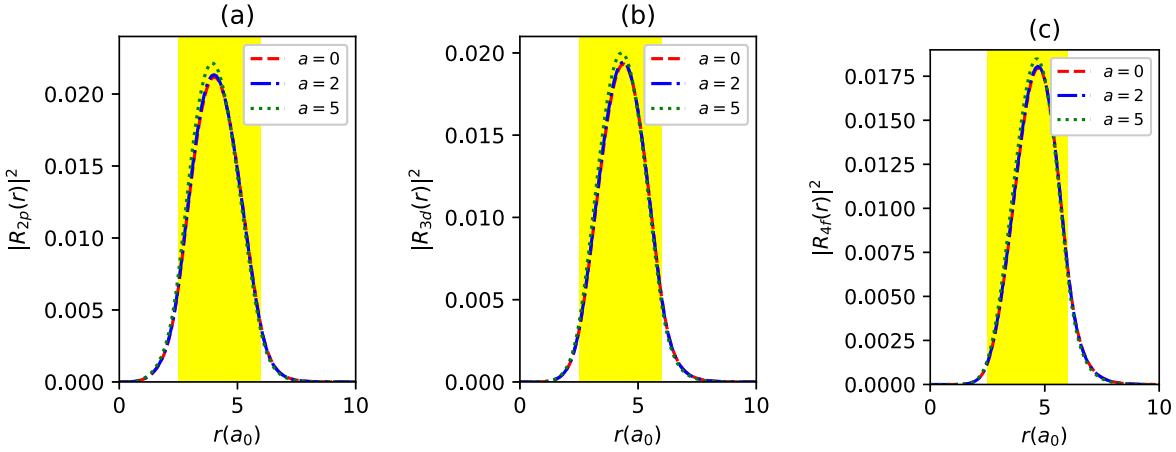

Figure 7. The radial density probabilities of $2p$ (a), $3d$ (b) and $4f$ states (c) with spin up for different a values in synchronization with the parameter set in figure 6, as a function of r. The colored regions are the endohedral cage locations.

Table 3. Energy values for the a-change of some quantum states in synchronization with the parameter set in figure 1(c).

	a					
Energy (eV)	0	1	2	3	4	5
$-E_{1s}$	48.162 304 9	48.126 379	48.019 211	47.842 604	47.599 517	47.293 989
$-E_{2p\uparrow}$	45.469 877	45.425 905	45.294 458	45.076 916	44.775 521	44.393 286
$-E_{2p\downarrow}$	45.471 536	45.427 561	45.296 102	45.078 542	44.777 123	44.394 858
$-E_{3d\uparrow}$	41.774 405	41.725 028	41.577 395	41.332 970	40.994 129	40.564 061
$-E_{3d\downarrow}$	41.775 609	41.726 230	41.578 589	41.334 152	40.995 293	40.565 205
$-E_{4f\uparrow}$	37.143 814	37.088 719	36.923 983	36.651 231	36.273 084	35.793 054
$-E_{4f\downarrow}$	37.144 983	37.089 886	36.925 144	36.652 382	36.274 222	35.794 176
$-E_{5g\uparrow}$	31.841 425	31.780 344	31.597 747	31.295 528	30.876 724	30.345 358
$-E_{5g\downarrow}$	31.842 649	31.781 567	31.598 966	31.296 741	30.877 929	30.346 552

levels is demonstrated in table 5. It is observed that as the endohedral cage width increases, energy levels decrease, leading the system towards greater stability. Figure 10 illustrates the PC and IMF responses originating from the $2p$, $3d$, and $4f$ levels for spin up and spin down orientations concerning the increase in the endohedral fullerene width D. As observed, there is a significant decrease in the I–B characteristics due to the increase in the endohedral fullerene width D. Figure 11 shows the RDP of $2p$, $3d$, and $4f$ as a function of r for increasing values of the endohedral fullerene

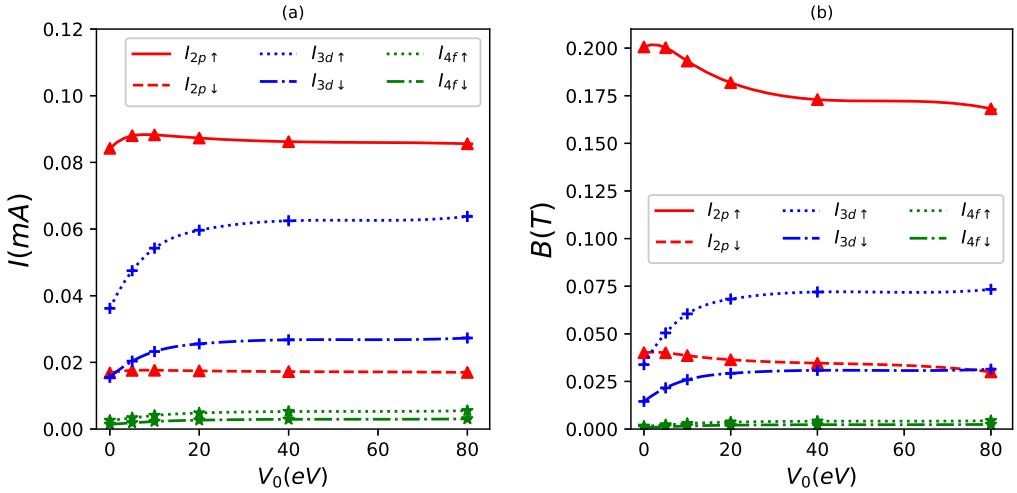

Figure 8. Persistent currents (a) and induced magnetic fields (b) as a function of V_0 for some quantum states in synchronization with the parameter set in figure 1(d).

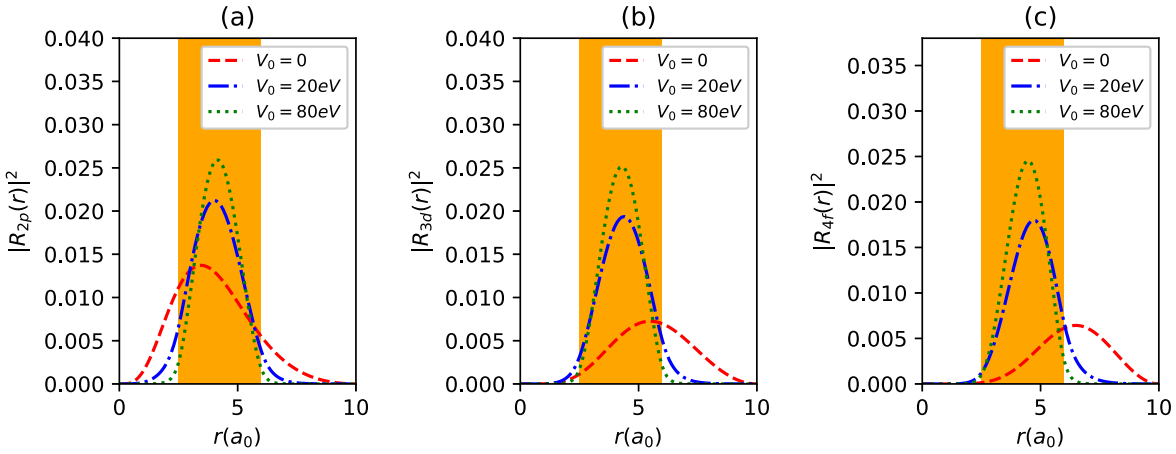

Figure 9. The radial density probabilities of $2p$ (a), $3d$ (b) and $4f$ states (c) with spin up for different V_0 values in synchronization with the parameter set in figure 8, as a function of r. The colored regions are the endohedral cage locations.

Table 4. Energy values for the V_0-change of some quantum states in synchronization with the parameter set in figure 1(d).

	V_0(eV)					
Energy (eV)	0	5	10	20	30	40
$-E_{1s}$	39.988 977	40.738 897	42.077 558	48.126 379	56.787 282	66.069 451
$-E_{2p\uparrow}$	28.700 219	32.469 805	36.592 022	45.425 905	54.672 085	64.130 105
$-E_{2p\downarrow}$	28.700 297	32.469 996	36.592 550	45.427 561	54.675 328	64.135 591
$-E_{3d\uparrow}$	25.137 047	28.615 772	32.748 726	41.725 028	51.077 797	60.604 703
$-E_{3d\downarrow}$	25.137 069	28.615 940	32.749 172	41.726 230	51.079 928	60.607 893
$-E_{4f\uparrow}$	22.291 786	24.868 145	28.480 711	37.088 719	46.336 573	55.825 394
$-E_{4f\downarrow}$	22.291 799	24.868 300	28.481 158	37.089 886	46.338 548	55.828 241
$-E_{5g\uparrow}$	19.415 901	21.146 414	23.954 580	31.780 344	40.733 353	50.075 335
$-E_{5g\downarrow}$	19.415 911	21.146 541	23.955 015	31.781 567	40.735 403	50.078 240

width D. An increase in the endohedral fullerene width results in the electron localizing over a wider area, which is expected to cause a decrease in the RDP. Additionally, the electron moves radially away from the center, supporting the decrease in the PC and IMF due to the diminishing RDP, ultimately leading to the prominent $I-B$ characteristics observed in figure 10.

Figure 1(f) depicts the variation in the interaction potential as function of the inner radius of the endohedral cage (R_c) and the radial variable (r). Table 6 presents the energy values of

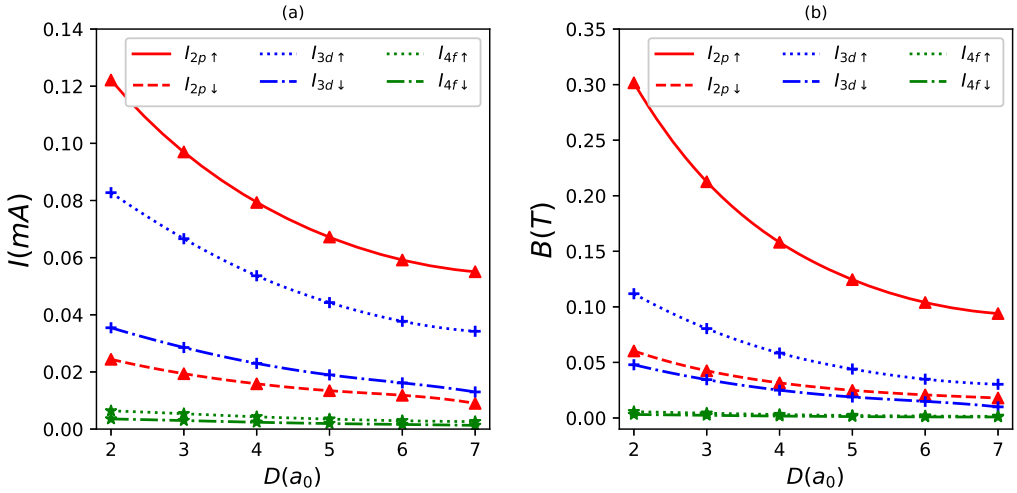

Figure 10. Persistent currents (a) and induced magnetic fields (b) as a function of D for some quantum states in synchronization with the parameter set in figure 1(e).

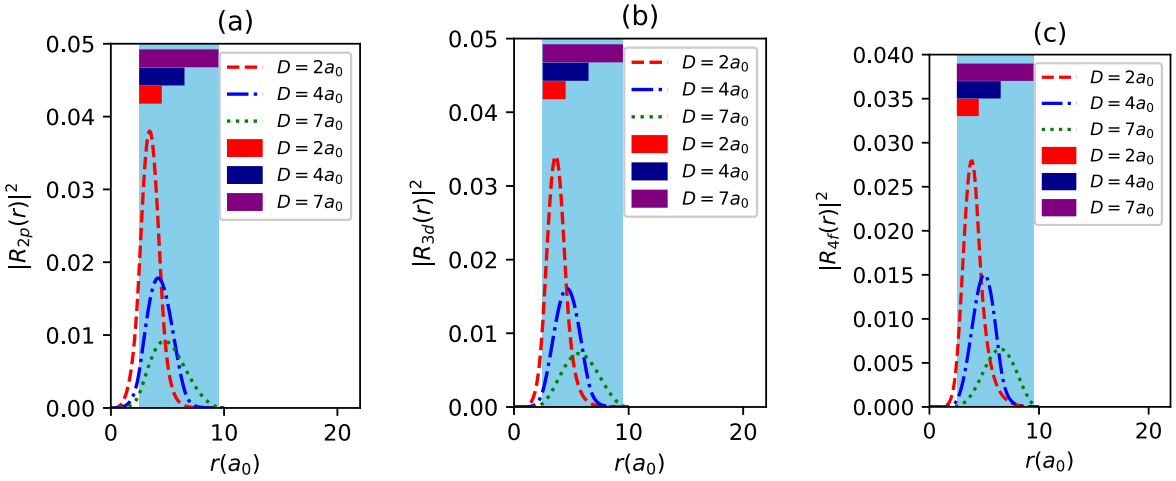

Figure 11. The radial density probabilities of $2p$ (a), $3d$ (b) and $4f$ states (c) with spin up for different D values in synchronization with the parameter set in figure 10, as a function of r. The colored regions are the endohedral cage locations.

Table 5. Energy values for the D-change of some quantum states in synchronization with the parameter set in figure 1(e).

	$D(a_0)$					
Energy (eV)	2.5	3	3.5	4	5	6
$-E_{1s}$	46.921 265	47.627 100	48.126 379	48.474 227	48.877 592	49.059 312
$-E_{2p\uparrow}$	43.371 295	44.577 101	45.425 905	46.027 627	46.763 044	47.132 761
$-E_{2p\downarrow}$	43.373 663	44.579 078	45.427 561	46.029 019	46.764 042	47.133 480
$-E_{3d\uparrow}$	38.786 692	40.478 537	41.725 028	42.653 036	43.878 439	44.574 271
$-E_{3d\downarrow}$	38.788 304	40.479 927	41.726 230	42.654 078	43.879 225	44.574 829
$-E_{4f\uparrow}$	32.999 393	35.305 532	37.088 719	38.475 516	40.419 585	41.617 762
$-E_{4f\downarrow}$	33.000 807	35.306 821	37.089 886	38.476 571	40.420 444	41.618 414
$-E_{5g\uparrow}$	26.419 586	29.370 098	31.780 344	33.724 784	36.562 074	38.392 075
$-E_{5g\downarrow}$	26.420 898	29.371 389	31.781 567	33.725 928	36.563 055	38.392 846

certain quantum levels, including spin up and spin down orientations. The change in R_c forms a repulsive potential characteristic for the $1s$ and $2p$ energy levels, an attractive characteristic for $4f$ and $5g$, and an initially attractive ($R_c \simeq 3a_0$) and then repulsive characteristic for $3d$. Figure 12 illustrates the behavior of the PC and IMF as a function of R_c. Although an increase in R_c creates an unstable response in the localization of certain energy levels, it causes a stable impact on the PC and IMF. The increase in the inner radius of the endohedral cage significantly decreases the PC and IMF (see

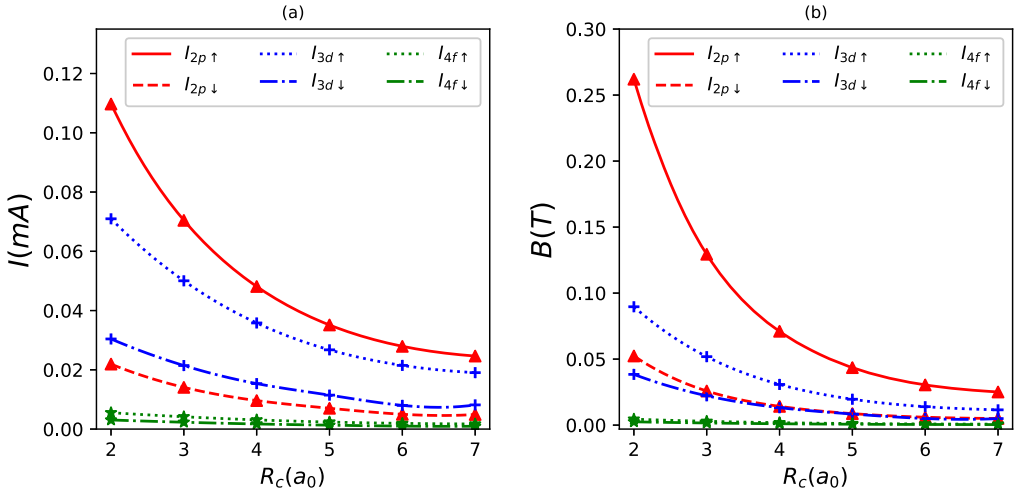

Figure 12. Persistent currents (a) and induced magnetic fields (b) as a function of R_c for some quantum states in synchronization with the parameter set in figure 1(f).

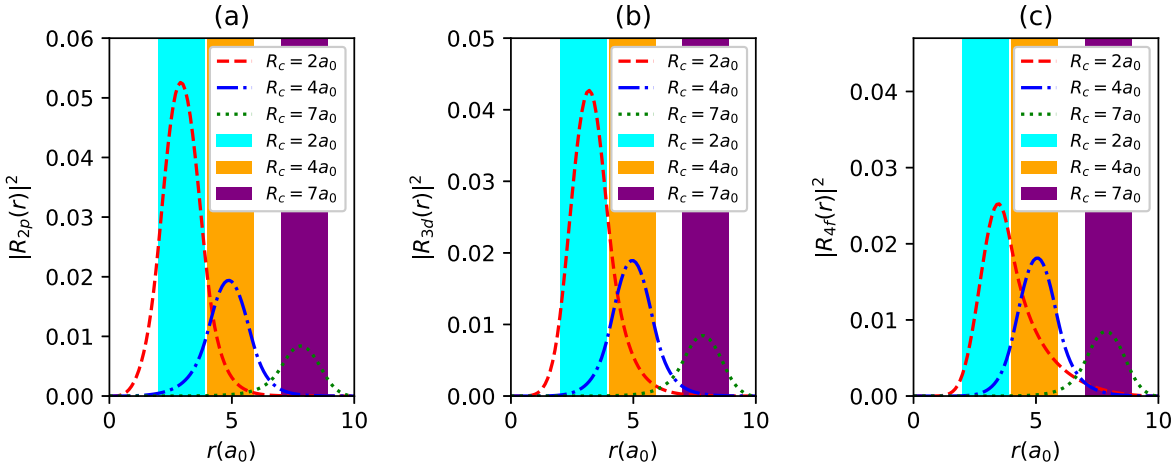

Figure 13. The radial density probabilities of $2p$ (a), $3d$ (b) and $4f$ states (c) with spin up for different R_c values in synchronization with the parameter set in figure 12, as a function of r. The colored regions are the endohedral cage locations.

Table 6. Energy values for the R_c-change of some quantum states in synchronization with the parameter set in figure 1(f).

	$R_c(a_0)$					
Energy (eV)	2.5	3	3.5	4	4.5	5
$-E_{1s}$	48.126 379	46.838 977	45.838 567	45.033 708	44.355 463	43.738 906
$-E_{2p\uparrow}$	45.425 905	44.919 674	44.420 278	43.944 126	43.487 505	43.024 168
$-E_{2p\downarrow}$	45.427 561	44.921 733	44.422 819	43.947 226	43.491 244	43.028 630
$-E_{3d\uparrow}$	41.725 028	41.996 429	42.073 720	42.026 291	41.891 154	41.670 046
$-E_{3d\downarrow}$	41.726 230	41.997 772	42.075 257	42.028 064	41.893 186	41.672 316
$-E_{4f\uparrow}$	37.088 719	38.146 105	38.867 048	39.335 035	39.608 013	39.706 681
$-E_{4f\downarrow}$	37.089 886	38.147 304	38.868 326	39.336 431	39.609 549	39.708 341
$-E_{5g\uparrow}$	31.780 344	33.581 400	34.955 272	35.978 111	36.711 330	37.183 243
$-E_{5g\downarrow}$	31.781 567	33.582 605	34.956 491	35.979 376	36.712 661	37.184 626

figure 12). Figure 13 explains the behavior of the RDP of $2p$, $3d$, and $4f$ as a function of the radial variable (r) for different locations of the endohedral cage along the radial axis or, specifically, for an increasing inner radius. As observed, as the inner radius increases, both the electron's RDP decreases and it moves away from the radial center. These two outcomes, having a diminishing effect on the PC and IMF, complement each other, ultimately resulting in a notably decreasing I–B characteristic. Figure 1(g) explains the response due to the smoothing effect of the endohedral fullerene capsulation. As

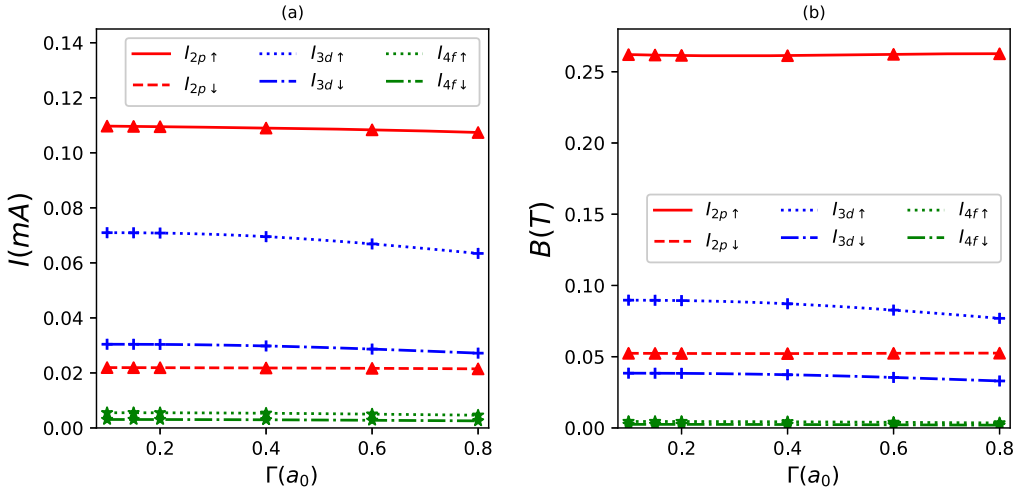

Figure 14. Persistent currents (a) and induced magnetic fields (b) as a function of Γ for some quantum states in synchronization with the parameter set in figure 1g.

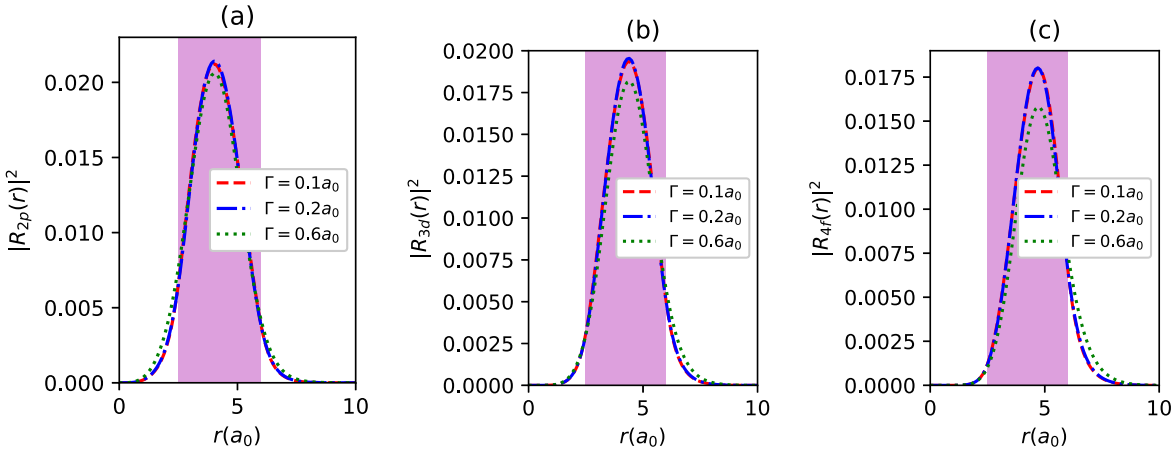

Figure 15. The radial density probabilities of $2p$ (a), $3d$ (b) and $4f$ states (c) with spin up for different Γ values in synchronization with the parameter set in figure 14, as a function of r. The colored regions are the endohedral cage locations.

Table 7. Energy values for the Γ-change of some quantum states in synchronization with the parameter set in figure 1(g).

	$\Gamma(a_0)$					
Energy (eV)	0.1	0.2	0.3	0.4	0.5	0.6
$-E_{1s}$	48.126 379	47.881 460	47.547 542	47.182 011	46.841 177	46.566 542
$-E_{2p\uparrow}$	45.425 905	45.108 175	44.630 063	44.033 354	43.365 404	42.670 114
$-E_{2p\downarrow}$	45.427 561	45.109 029	44.630 672	44.033 843	43.365 810	42.670 450
$-E_{3d\uparrow}$	41.725 028	41.406 715	40.919 619	40.304 372	39.610 619	38.885 777
$-E_{3d\downarrow}$	41.726 230	41.407 357	40.920 084	40.304 751	39.610 940	38.886 051
$-E_{4f\uparrow}$	37.088 719	36.777 899	36.309 170	35.724 994	35.075 309	34.406 898
$-E_{4f\downarrow}$	37.089 886	36.778 524	36.309 622	35.725 361	35.075 619	34.407 164
$-E_{5g\uparrow}$	31.780 344	31.478 579	31.046 868	30.532 894	29.983 593	29.439 173
$-E_{5g\downarrow}$	31.781 567	31.479 231	31.047 334	30.533 267	29.983 905	29.439 438

observed, as the smoothing increases, the interaction potential gains a repulsive characteristic, leading to a stable trend in terms of the localization of bound states. Table 7 illustrates the changes in the energy levels of quantum states due to smoothing. It is observed that as Γ increases, the endohedral fullerene capsulation exhibits a more unstable confining tendency, consequently resulting in a decrease in bound-state energies. However, this decrease is not very pronounced but rather follows a monotonic form. This monotonicity is also reflected in the PC and IMF characteristics (see figure 14). In a more repulsive potential, the probabilities of bound-state localizations are weaker. As depicted in figure 15, as Γ

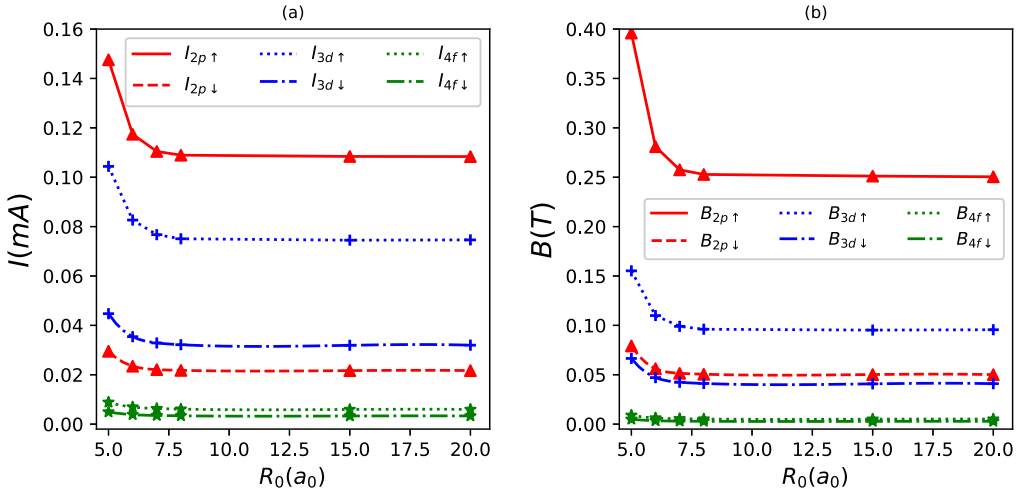

Figure 16. Persistent currents (a) and induced magnetic fields (b) as a function of R_0 for some quantum states, when $\lambda = 80a_0$, $b = 1/a_0$, $a = 1$, $V_0 = 20$ eV, $D = 2.5a_0$, $R_c = 2.5a_0$, and $\Gamma = 0.1a_0$.

Table 8. Energy values for the R_0-change of some quantum states when $\lambda = 80a_0$, $b = 1/a_0$, $a = 1$, $V_0 = 20$ eV, $D = 3.5a_0$, $R_c = 2.5a_0$, and $\Gamma = 0.1a_0$.

	$R_0(a_0)$					
Energy (eV)	3	5	9	11	15	20
$-E_{1s}$	38.324 953	45.126 285	48.125 575	48.126 444	48.126 450	48.126 450
$-E_{2p\uparrow}$	14.405 374	39.832 223	45.423 953	45.426 087	45.426 105	45.426 105
$-E_{2p\downarrow}$	14.406 259	39.833 028	45.425 606	45.427 743	45.427 761	45.427 761
$-E_{3d\uparrow}$	–	33.705 014	41.720 405	41.725 555	41.725 620	41.725 620
$-E_{3d\downarrow}$	–	33.705 372	41.721 605	41.726 757	41.726 823	41.726 823
$-E_{4f\uparrow}$	–	25.768 276	37.076 815	37.090 487	37.090 787	37.090 787
$-E_{4f\downarrow}$	–	25.768 464	37.077 979	37.091 654	37.091 954	37.091 954
$-E_{5g\uparrow}$	–	16.168 733	31.748 698	31.786 902	31.788 620	31.788 623
$-E_{5g\downarrow}$	–	16.168 836	31.749 918	31.788 125	31.789 842	31.789 845

increases, the RDPs of $2p$, $3d$, and $4f$ show a slight decrease, which equally affects the PC and IMF characteristics (see figure 15). Table 8 presents the energies of certain quantum levels, depending on the increase in the spherical confinement effect (R_0). As observed, the effective range of the spherical confinement concerning the energy levels of bound states is approximately $0-9a_0$. As R_0 increases, the quantum levels decrease. However, outside this effective range, there is almost no change in energy levels. Figure 16 demonstrates the changes in the PC and IMF as a function of the spherical confinement effect. It is evident that as the spherical confinement range decreases, the electron's RDP decreases significantly. This decrease results in very clear reductions in the PC and IMF within the effective range of R_0 (see figure 17).

Table 9 illustrates the effect of the increase in the magnetic quantum number (m) on the PC and IMF. As observed, this effect arising from spherical harmonics is weak because the interaction potential does not have angular dependence. An increase in the magnetic quantum number (m) leads to angular probability densities localizing more towards the xy-plane rather than the z-axis. Consequently, an increase in angular probability and, therefore, an increase in the PC and IMF could be expected. However, the current integration might not provide a stable response to the increase in m due to angular normalization coefficients and Clebsch–Gordan coefficients. Therefore, the results originating from some numerical cases might predominate in the increment of the angular probability when considering the PC and IMF. In summary, the study delves into the intricate interplay among different parameters affecting the PCs and IMFs of quantum plasma-encased endohedral fullerenes. The results show a nuanced dependence on these parameters, with certain regimes leading to enhanced or reduced PCs and magnetic fields. The interplay of plasma screening, endofullerene encapsulation, spherical confinement, and other factors adds a layer of complexity to the behavior of these quantum systems. The detailed analysis and presentation of results provide insights into the underlying physics and potential applications of such systems in quantum information processing and other fields.

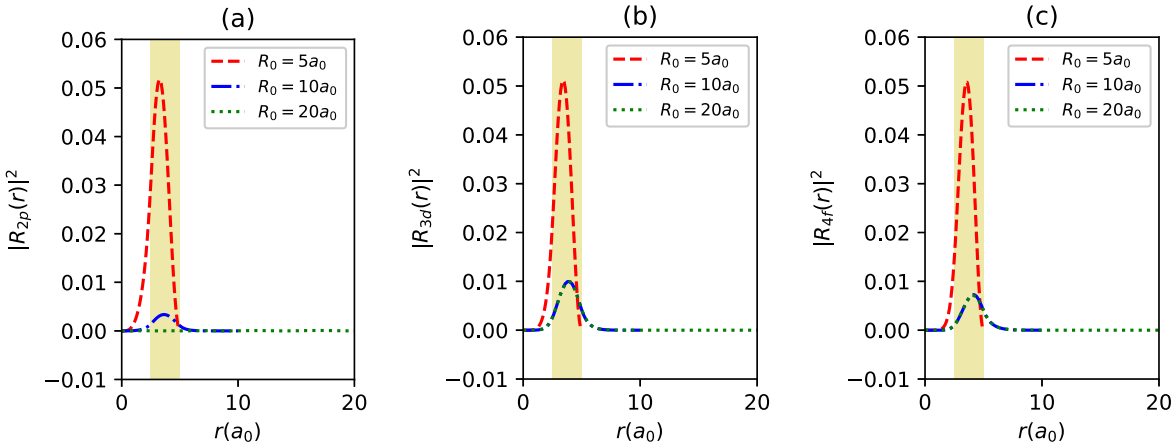

Figure 17. The radial density probabilities of $2p$ (a), $3d$ (b) and $4f$ states (c) with spin up for different Γ values, when $\lambda = 80a_0$, $b = 1/a_0$, $a = 1$, $V_0 = 20$ eV, $D = 2.5a_0$, $R_c = 2.5a_0$, and $\Gamma = 0.1a_0$, as a function of r. The colored regions are the endohedral cage locations.

Table 9. The magnetic quantum number (m) effect on the PC and IMF, when $\lambda = 80a_0$, $b = 1/a_0$, $a = 1$, $V_0 = 20$ eV, $D = 3.5a_0$, $R_c = 2.5a_0$, $\Gamma = 0.1a_0$, and $R_0 = 10a_0$.

$\|n\ell m_\ell m_s\rangle$	$I(mA)$	$B(T)$
$\|111 + 1/2\rangle$	0.087 317	0.181 876
$\|111 - 1/2\rangle$	0.017 464	0.036 404
$\|122 + 1/2\rangle$	0.019 171	0.043 876
$\|122 - 1/2\rangle$	0.002 130	0.004 875
$\|121 + 1/2\rangle$	0.059 643	0.068 252
$\|121 - 1/2\rangle$	0.025 561	0.029 254
$\|133 + 1/2\rangle$	0.000 115	0.000 263
$\|133 - 1/2\rangle$	0.000 008	0.000 020
$\|132 + 1/2\rangle$	0.005 802	0.008 795
$\|132 - 1/2\rangle$	0.001 582	0.002 398
$\|131 + 1/2\rangle$	0.004 809	0.003 645
$\|131 - 1/2\rangle$	0.002 671	0.002 024

4. Concluding remarks

As expected, while spin orientations create a very subtle difference in bound-state energies, there is a noticeable difference between the PC and IMF of spin up and down configurations when considering every parameter change. The values of I–B for spin up configurations are consistently larger. The difference between the spin up and down states is most significant for the PC and IMF of quantum levels closer to the hydrogen nucleus, diminishing as one moves away from the nucleus towards outer levels. The impact of the λ parameter is more pronounced on both the energies and I–B in weaker regimes, approximately around $\lambda \simeq 0$–$40a_0$. While the b screening parameter significantly affects bound-state energies, its effect on the PC and IMF is unexpectedly weak. Meanwhile, the a screening parameter has a weak effect on both the energies and the I–B characteristics. In terms of plasma functionality, the most effective and functional parameter for the PC and IMF is λ. This is advantageous from an experimental perspective as well because λ is a parameter that is dependent on plasma temperature T and plasma density n, allowing alterations in I–B characteristics with changes in n and T. An increase in the depth of endohedral fullerene encapsulation (V_0) affects the PC and IMF of $2p$ and $3d$–$4f$ levels in different ways. In this context, it has become evident in the analysis of V_0 that the I–B characteristic is not solely dependent on the current density ($\vec{J}$) but also on the electron's radial distance from the center. The effective range of V_0 for the PC and IMF has been determined to be 0–30 eV under the given conditions. As the endohedral fullerene expands (D), both the RDP decreases and the electron moves away from the radial center. Consequently, an increase in D effectively reduces I–B values. The inner radius of the endofullerene (R_c) stands out as the most significant and functional parameter for the PC and IMF. In this regard, it could be an alternative to D. The effect of smoothing (Γ) effect should be considered as a fine-tuning parameter for the PC and IMF of endofullerenes. This is because smoothing requires less experimental effort and has a very weak impact on I–B characteristics. The spherical confinement (R_0) also affects the PC and IMF. However, for the numerical values within the given parameter set, the functional range of R_0 is approximately 0–$10a_0$. Even without angular interactions, spherical harmonics influence the PC and IMF. However, the localization effect of Y_ℓ^m alone may not be the sole impactful factor in this influence.

Conflicts of interest/Competing interests

Mustafa Kemal Bahar is the only author of this study.

References

[1] Muller K H, Dunsch L, Eckert D, Wolf M and Bartl A 1999 Magnetic properties of endohedral fullerene complexes *Synth. Met.* **103** 2417

[2] Dallas P *et al* 2020 Magnetic properties of endohedral fullerenes: applications and perspectives *21st Century Nanoscience A Handbook: Low-Dimensional Materials and Morphologies* (CRC Press) Vol. 4, 16

[3] Powell W H, Cozzi F, Moss G P, Thilgen C, Hwu R R and Yerin A 2002 Nomenclature for the C60-Ih and C70-D5h (6) fullerenes (IUPAC Recommendations 2002) *Pure Appl. Chem.* **74** 629

[4] Hiorns R C, Cloutet E, Ibarboure E, Khoukh A, Bejbouji H, Vignau L and Cramail H 2010 Synthesis of donor acceptor multiblock copolymers incorporating fullerene backbone repeat units *Macromolecules* **43** 6033

[5] Ju C, Sriter D and Du J 2007 Two-qubit gates between noninteracting qubits in endohedral-fullerene-based quantum computation *Phys. Rev.* A **75** 012318

[6] Becker L, Poreda R J and Bunch T E 2000 Fullerenes: an extraterrestrial carbon carrier phase for noble gases *Proceedings of the National Academy of Sciences* 97 2979

[7] Matsuo Y, Okada H and Ueno H 2017 *Endohedral Lithium-containing Fullerenes* (Springer) vol. 1

[8] Yang S 2014 *Endohedral Fullerenes: From Fundamentals to Applications* (World Scientific)

[9] Martin N and Guldi M D (ed) 2010 *Carbon Nanotubes and Related Structures: Synthesis, Characterization, Functionalization, and Applications* (Wiley)

[10] Dolmatov V K, Baltenkov A, Connerade J-P and Manson S 2004 Structure and photoionization of confined atoms *Radiat. Phys. Chem.* **70** 417

[11] Motapon O, Ndengue S A and Sen K D 2011 Static and dynamic dipole polarizabilities and electron density at origin: ground and excited states of hydrogen atom confined in multiwalled fullerenes *Int. J. Quantum Chem.* **111** 4425

[12] Dolmatov V K and Edwards A 2019 Role of polarizability of a CN fullerene cage in A@CN photoionization and eCN scattering: the size effect *J. Phys. B: At. Mol. Opt. Phys.* **52** 105001

[13] Dubey K A, Srikanth K, Rao T R and Jose J 2020 Effects of anisotropy on the resonant scattering of Hydrogen atom from the fullerene C60 *Comput. Phys. Commun.* **4** 075016

[14] Ndengue S A and Motapon O 2008 Electric response of endohedrally confined hydrogen atoms *J. Phys. B: At. Mol. Opt. Phys.* **41** 045001

[15] Martinez-Flores C 2021 Shannon entropy and Fisher information for endohedral confined one-and two-electron atoms *Phys. Lett.* A **386** 126988

[16] Wu L, Zhang S and Li B 2020 Fisher information for endohedrally confined hydrogen atom *Phys. Lett.* A **384** 126033

[17] Bonizzoni G and Vassallo E 2002 Plasma physics and technology; industrial applications *Vacuum* **64** 327

[18] Janev R K, Zhang S and Wang J 2016 Review of quantum collision dynamics in Debye plasmas *Matter Radiat. Extremes* **1** 237

[19] Fridman A and Kennedy L A 2021 *Plasma Physics and Engineering* (CRC Press)

[20] Neyts E C and Brault P 2017 Molecular dynamics simulations for plasma surface interactions *Plasma Processes Polym.* **14** 1600145

[21] Soylu A 2012 Plasma screening effects on the energies of hydrogen atom *Phys. Plasmas* **19** 072701

[22] Bahar M K 2015 Effects of laser radiation field on energies of hydrogen atom in plasmas *Phys. Plasmas* **22** 092709

[23] Bahar M K and Soylu A 2016 Probe of hydrogen atom in plasmas with magnetic, electric, and Aharonov–Bohm flux fields *Phys. Plasmas* **23** 092712

[24] Martinez-Flores C and Cabrera-Trujillo R 2018 Dipole and generalized oscillator strength derived electronic properties of an endohedral hydrogen atom embedded in a Debye–Hückel plasma *Matter Radiat. Extremes* **3** 227

[25] Bahar M K and Martinez-Flores C 2023 Photoionization cross section for $H@C_n$ implanted in nonideal classical plasmas *Ann. Phys.* **535** 230018

[26] Svoboda J 2004 *Magnetic Techniques for the Treatment of Materials* 1st edn (Kluwer)

[27] Radu I *et al* 2011 Transient ferromagnetic-like state mediating ultrafast reversal of antiferromagnetically coupled spins *Nat. Phys.* **472** 205

[28] Zhang G P, Lefkidis G, Hübner W and Bai Y 2012 Manipulating femtosecond magnetization in ferromagnets and molecular magnets through laser chirp *J. Appl. Phys.* **111** 07C508

[29] Zhang G P, Hübner W, Lefkidis G, Bai Y and George T F 2009 Paradigm of the time-resolved magneto-optical Kerr effect for femtosecond magnetism *Nat. Phys.* **5** 499

[30] Helmerson K, Andersen M F, Ryu C, Cladéa P, Natarajan V, Vaziri A and Phillips W D 2007 Generating persistent currents states of atoms using orbital angular momentum of photons *Nucl. Phys.* A **790** 705c

[31] Watzel J, Pavlyukh Y, Schaffer A and Berakdar J 2016 Optical vortex driven charge current loop and optomagnetism in fullerenes *Carbon* **99** 439

[32] Köksal K and Berakdar J 2012 Charge-current generation in atomic systems induced by optical vortices *Phys. Rev.* A **86** 063812

[33] Manabe D and Koizumi H 2019 Supercurrent generation by spin-twisting itinerant motion of electrons *J. Supercond. Novel Magn.* **32** 2303

[34] Matos-Abiague A and Berakdar J 2005 Photoinduced charge currents in mesoscopic rings *Phys. Rev. Lett.* **94** 166801

[35] Moskalenko A S and Berakdar J 2009 Light-induced valley currents and magnetization in graphene rings *Phys. Rev.* B **80** 193407

[36] Barth I and Manz J 2007 Electric ring currents in atomic orbitals and magnetic fields induced by short intense circularly polarized π laser pulses *Phys. Rev.* A **75** 012510

[37] Talwar S L, Lumb S and Prasad V 2021 Charge currents and induced magnetic fields in a bounded two-dimensional hydrogen atom *Eur. Phys. J.*D **59** 75

[38] Lumb S, Talwar S L and Prasad V 2020 Generation of charge currents and magnetic pulses *J. Phys. B: At. Mol. Opt. Phys.* **53** 205002

[39] Prasad V, Lumb S, Talwar S L, Lefkidis G and Hübner W 2019 Confinement effects on persistent currents in hydrogenic atoms *Phys. Scr.* **94** 125015

[40] Prasad V, Talwar S L, Lumb S, Lefkidis G and Hübner W 2019 Persistent currents and induced magnetization in presence of external magnetic field and transition probabilities in presence of combined laser pulse and external magnetic field for a confined hydrogen atom *Phys. Lett.* A **383** 125775

[41] Zutic I, Fabian J and Sarma S D 2004 Spintronics: fundamentals and applications *Rev. Mod. Phys.* **76** 323

[42] Bernevig B A 2013 *Topological Insulators and Topological Superconductors* (Princeton University Press)

[43] Greiner W 2000 *Relativistic Quantum Mechanics* 3rd edn (Springer)

[44] Cooper F, Khare A and Sukhatme U 1995 Supersymmetry and quantum mechanics *Phys. Rep.* **251** 267

[45] Martin P C and Glauber R J 1958 Relativistic theory of radiative orbital electron capture *Phys. Rev.* **109** 1307

[46] Barthelat J C, Pelisser M and Durand P H 1980 Analytical relativistic self-consistent-field calculations for atoms *Phys. Rev.* A **21** 1773

[47] Baym G 1969 *Lectures on Quantum Mechanics* (CRC Press)

[48] Kutzelnigg W 1984 Basis set expansion of the Dirac operator without variational collapse *Int. J. Quantum Chem.* **25** 107

[49] Karwowski J and Kobus J 1985 Quasirelativistic methods *Int. J. Quantum Chem.* **28** 741

[50] Biedenham L C 1983 The 'Sommerfeld Puzzle' revisited and resolved *Found. Phys.* **13** 13
[51] Biedenharn L C 1962 Remarks on the relativistic Kepler problem *Phys. Rev.* **126** 845
[52] Steven C C and Raymond P C 1990 *Numerical Methods for Engineers* (McGraw-Hill)
[53] Deshmukh1 P C, Jose J, Varma H R and Manson S T 2021 Electronic structure and dynamics of confined atoms *Eur. Phys. J.* D **75** 166
[54] Dolmatov V K, King J L and Oglesby J C 2012 Diffuse versus square-well confining potentials in modelling A@ C60 atoms *J. Phys. B: At. Mol. Opt. Phys.* **45** 105102
[55] Bahar M K 2015 Effects of laser radiation field on energies of hydrogen atom in plasmas *Phys. Plasmas* **22** 092709
[56] Barth I and Manz J 2007 Electric ring currents in atomic orbitals and magnetic fields induced by short intense circularly polarized π laser pulses *Phys. Rev.* A **75** 012510
[57] Greiner W and Physik T 2005 *Bd. 4: Quantenmechanik: Einfhrung* (Verlag Harri Deutsch)
[58] Bahar M K 2021 Charge-current output in plasma-immersed hydrogen atom with noncentral interaction *Ann. Phys.* **533** 2100111
[59] Poszwa A and Bahar M K 2015 Relativistic corrections for screening effects on the energies of hydrogen-like atoms embedded in plasmas *Phys. Plasmas* **22** 012104
[60] Paul S and Ho Y K 2009 Hydrogen atoms in Debye plasma environments *Phys. Plasmas* **16** 063302
[61] Sever R and Tezcan C 1987 $1/N$ expansion for the exponential-cosine-screened Coulomb potential *Phys. Rev.* A **35** 2725